PHYSICAL REVIEW B **89**, 201107(R) (2014)

First-principles study of octahedral tilting and ferroelectric-like transition in metallic $LiOsO_3$

Hyunsu Sim and Bog G. Kim*

Department of Physics, Pusan National University, Pusan 609-735, South Korea

(Received 17 November 2013; revised manuscript received 17 April 2014; published 12 May 2014)

The octahedral tilting and ferroelectric-like structural transition of $LiOsO_3$ metallic perovskite [Y. Shi *et al.*, Nat. Mater. **12**, 1024 (2013)] is studied using first-principles density-functional theory. In $LiOsO_3$, the $a^-a^-a^-$ octahedral tilting mode is responsible for cubic ($Fm\bar{3}m$) to rhombohedral structure ($R\bar{3}c$), which is stable phase at room temperature, and at low temperature, noncentrosymmetric transition to $R3c$ rhombohedral transition is realized as a result of zone center phonon softening. By using density-functional calculation and phonon calculation, the phase transition behavior of $LiOsO_3$ can be fully understood. We also present electronic structure change and Fermi surface change due to electron lattice coupling effect. The change of carrier density of state across phase transition is associated with experimental temperature dependence of resistivity, heat capacity, and susceptibility.

DOI: 10.1103/PhysRevB.89.201107 PACS number(s): 71.15.Mb, 61.50.Ah, 63.20.dk, 77.84.Ek

Recently, there has been considerable interest in octahedral tilting transition and noncentrosymmetric transition in perovskite oxides not only for their technological importance as new ferroelectric materials and multistage memory devices but also from a fundamental point of view [1–4]. In this pursuit, first-principles density-functional theory has played a key role in explaining new physical states as well as predicting new realizations of physical states of materials [5–7]. $LiOsO_3$ is one of the important and unique additions to a new oxide material with pervoskite structure. According to a recent report from Shi *et al.* [8], $LiOsO_3$ is a perovskite oxide material with metallic properties. Interestingly, around 140 K, a centrosymmetric ($R\bar{3}c$) phase to noncentrosymmetric ($R3c$) phase transition is reported. They also reported an anomaly in temperature dependence of heat capacity, susceptibility, and resistivity and indicate that such a structural phase transition is equivalent to the ferroelectric transition of $LiNbO_3$ materials.

In both centrosymmetric ($R\bar{3}c$) and non-centrosymmetric ($R3c$) phases, the octahedral tilting is one of the important ingredients [9–12]. The three-dimensional network of OsO_6 octaheral tilting in $LiOsO_3$ can be easily characterized by Glazer notation [9]. Glazer notation describes the octahedral tilting using the symbol $a^\#b^\#c^\#$, in which the literals refer to tilt around the [100], [010], and [001] directions of the cubic perovskite, and the superscript # takes the value 0, +, or − to indicate no tilt or tilts of successive octahedra in the same or opposite sense. The rhombohedral ($R\bar{3}c$ and $R3c$) structure of $LiOsO_3$ can be classified by $a^-a^-a^-$ tilting [8,9]. This tilting of $LiOsO_3$ is basically the same as $LiNbO_3$ [13–20] and originates from the rigidity of the OsO_6 octahedron and the large ionic size difference of the Li and Os ions.

In addition to octahedral tilting, the zone center soft mode is the main source of the centrosymmetric ($R\bar{3}c$) and noncentrosymmetric ($R3c$) phases. In $LiNbO_3$, the phase transition from a centrosymmetric ($R\bar{3}c$) to a noncentrosymmetric ($R3c$) phase occurs around 1480 K [1,13,19]. And this phase transition is closely related to the softening of the A_{2u} infrared active phonon mode, which is involved in the movement of Li ions and off-centering of Nb ions [13–20]. Parinski *et al.* [13] successfully applied first-principles density-functional calculation for an explanation of phase transition in $LiNbO_3$ materials. Ping and Cohen [20] used molecular dynamics with a first-principles-based potential.

Here, we report a detailed analysis of the octahedral tilting and noncentrosymmetric phase transition of $LiOsO_3$ materials. We optimized the structure by using first-principles calculation. Then, a quantitative analysis has been applied to the octahedral tilting. Next we also calculate the phonon dispersion curve by using frozen phonon calculations [13–15]. Our analysis shows that the soft A_{2u} mode at the zone center is indeed responsible for the noncentrosymmetric transition in $LiOsO_3$ and also the importance of spontaneous symmetry breaking in this material. Finally, the electronic structure and Fermi surface topology of each phase and their relationship are examined.

We performed the first-principles calculations with the Perdew-Burke-Ernzerhof generalized gradient approximation (PBE GGA) [21] to the density-functional theory and the projector augmented-wave method as implemented in VASP [22,23]. We considered the following valence electron configurations: $1s^22s^1$ for Li, $5d^76s^1$ for Os, and $2s^22p^4$ for oxygen. Electronic wave functions are expanded with plane waves up to a kinetic-energy cutoff of 400 eV except for structural optimization, where a kinetic-energy cutoff of 500 eV has been applied in order to reduce the effect of Pulay stress. Momentum space integration is performed using $12 \times 12 \times 12$ Γ-centered Monkhorst-Pack k-point mesh [24]. With the given symmetry of perovskite imposed, lattice constants and internal coordinates were fully optimized until the residual Hellmann-Feynman forces became smaller than 10^{-4} eV/Å. In order to get the phonon dispersion curve and phonon partial density of state, frozen phonon calculation has been applied on a $2 \times 2 \times 2$ supercell (containing 80 atoms in superlattice configuration) using the PHONOPY program [25]. The ISOTROPY and AMPLIMODES programs were utilized to check the group-subgroup relationship and to quantify octahedral tilting as well as soft mode analysis [26,27]. In order to calculate Fermi surface topology, the Wannier interpolation technique is applied using the WANNIER90 program [28].

The rhombohedral phase of $LiOsO_3$ is shown in Fig. 1(a). Without any octahedral tilting [9], the $LiOsO_3$ structure is a

*boggikim@pusan.ac.kr

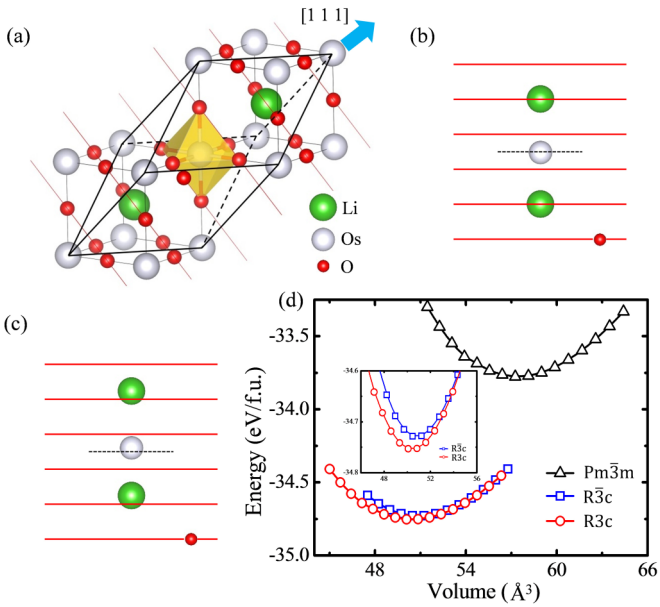

FIG. 1. (Color online) (a) The detailed room temperature structure of $LiOsO_3$ with space group 167, $R\bar{3}c$. Li, Os, and oxygen atoms are shown by green, gray, and red spheres, respectively. The oxygen plane is marked as a red line and the [111] direction of the pseudocubic notation is given as an arrow. (b) Schematic diagram of the oxygen plane vs Li and Os atoms in the [111] pseudocubic direction of the $R\bar{3}c$ phase. The Os atom is located in the center of two oxygen atoms. (c) Schematic diagram of the ferroelectric-like $R3c$ phase. In this projection, noncentrosymmetric nature is clearly shown by both Li and Os off-centering. (d) Total energy per formula unit as a function of the volume of the perovskite formula unit of the cubic, $R\bar{3}c$, and $R3c$ phases.

$Pm\bar{3}m$ cubic structure. With $a^-a^-a^-$ tilting [8,9], the $R\bar{3}c$ rhombohedral phase is stabilized and their unit cell can be viewed as $[a, a, 0]$, $[a, 0, a]$, and $[0, a, a]$ lattice vectors, where a is the lattice constant of the pseudocubic cell. Figures 1(b) and 1(c) depict the schematic diagram of two rhombohedral phases along the [111] axis of the pseudocubic lattice. In the centrosymmetric $R\bar{3}c$ rhombohedral phase, the Os atom locates in a symmetric position from two oxygen planes, which is also the central point connecting two Li atoms. Threefold rotation with mirror symmetry ($\bar{3}$) is due to oxygen octahedral tilting. Below the phase transition temperature, mirror symmetry is broken ($R3c$) because Os moves along the [111] axis, and the two oxygen planes are not equivalent to Os anymore. We calculated the energy per formula unit vs the volume per formula unit for three phases in Fig. 1(d). The lowest energy state is the noncentrosymmetric phase of $R3c$, where the total energy of $R\bar{3}c$ is 25 meV higher than that of $R3c$, and the total energy of the cubic phase is 978 meV higher than that of $R3c$. The lattice parameters as well as the Wyckoff position of each atom are summarized in Table I. The lattice parameters are slightly larger than those of the experimental values [8], which is common for GGA approximation. With this taken into account, our optimized structure reproduced quite well the experimental values of atomic position as well as the lattice parameters.

In order to see whether these phase transitions are spontaneous, we have computed the total energy of the system as a function of mode amplitude. Each mode related to the phase transition is calculated with the ISOTROPY and AMPLIMODES programs [26,27]. In the cubic to $R\bar{3}c$ transition, the relevant phonon mode is the $a^-a^-a^-$ tilting mode with an irreducible representation of R_{4+} [shown in Fig. 2(a)]. Figure 2(b) depicts the total energy vs mode amplitude of tilting, and angles for relevant tilting are also marked. The double-well shape energy related to tilting stabilization is quite large [$\sim$1.66 eV per formula unit for Fig. 2(b)] and it means that the transition to a parasitic cubic phase will not occur in ambient condition even at high temperature. The phase transition to the noncentrosymmetric $R3c$ phase is associated with an irreducible representation of Γ_{2-}, which is the mode of Os-O bending with Li displacement. As can be clearly seen from Fig. 2(d), the total energy of the system has a double-well-like shape with Γ_{2-} amplitude, which again indicates the spontaneous symmetry breaking. The energy related to the Γ_{2-} mode is about 47 meV per formula unit of perovskite and about 600 K in the temperature scale. This suggests that the experimental transition temperature of 140 K in $LiOsO_3$ is order-disorder type with a small ($\sim$25%) amount of displacive character. A quantitative analysis of two modes

TABLE I. Structural parameters and atomic Wyckoff position of $LiOsO_3$ for the two different phases ($R\bar{3}c$ and $R3c$). Here the volume is given for a standard conventional cell containing six pervoskite formula units and the angle is given for the O-Os-O bending angle. The experimental values from Ref. [8] are also given.

$LiOsO_3$		a (Å)	c (Å)	Volume (Å^3)	Angle (deg.)	Atom	Wyckoff site	x	y	z
$R\bar{3}c$						Li	6a	0.0	0.0	0.25
	Cal.	5.145	13.210	100.946	180	Os	6b	0.0	0.0	0.0
						O	18e	0.6278	0.0	0.25
						Li	6a	0.0	0.0	0.25
	Expt.	5.064	13.211	97.790	180	Os	6b	0.0	0.0	0.0
						O	18e	0.6298	0.0	0.25
$R3c$						Li	6a	0.0	0.0	0.2164
	Cal.	5.093	13.378	100.178	178.03	Os	6a	0.0	0.0	0.0
						O	18b	0.6296	−0.0339	0.2523
						Li	6a	0.0	0.0	0.2147
	Expt.	5.046	13.239	97.293	176.84	Os	6a	0.0	0.0	0
						O	18b	0.6260	−0.0102	0.2525

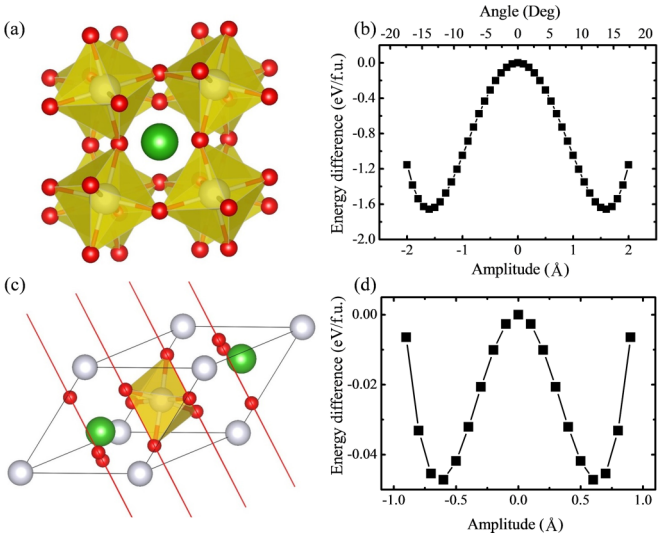

FIG. 2. (Color online) (a) Octahedral tilting ($a^-a^-a^-$) seen from the [111] pseudocubic axis. (b) Total energy variation as a function of octahedral tiling mode amplitude. The upper axis also shows the tilting angle of octahedra. (c) Γ_2-(A_{2u}) mode associated with the $R\bar{3}c$ to $R3c$ phase transition. (d) Total energy variation as a function of Γ_2-(A_{2u}) mode amplitude.

with R_{4+} and Γ_{2-} irreducible representation is summarized in Table II. The mode amplitude (1.6098 Å) is the minimum point in the double-well potential shown in Fig. 2(b) and the corresponding tilting angle is 14.11°. The reference structure for the Γ_{2-} mode is the rhombohedral structure of the $R\bar{3}c$ space group and this mode is composed of Os-O bending (Os and O atom displacement) and Li off-centering. The mode amplitude is 0.6010 Å and this is the value that can be obtained from Fig. 2(d). Compared to $LiNbO_3$ [13–15], the Li off-centering is nearly similar and the Os-O bending is smaller than the Nb-O bending mode.

Now let us turn our attention to phonon dispersion calculation. The phonon dispersion curves for the two phases are calculated with frozen phonon approximation. We have not considered longitudinal-optical–transverse-optical splitting because of the metallic nature of the system. Figures 3(a) and 3(b) depict the phonon dispersion curve along the high symmetry point of the Brillouin zone and the atom projected partial phonon density of state (PDOS) in the $R\bar{3}c$ phase. The negative y axis in Fig. 3(a) means the imaginary frequency mode, which is unstable in the given structure. The frequency of the zone center phonon is summarized in Supplemental Material Table S1 [29]. There are two imaginary frequency modes, A_{2g} and A_{2u}, at the zone center Γ point. Actually, an irreducible representation of the A_{2u} mode is the Γ_{2-} mode of Figs. 2(c) and 2(d). Note that the A_{2u} mode is a soft mode of the $LiNbO_3$ compound [13–16]. The A_{2u} mode is also related to the domain structure in the ferroelectric phase of $LiNbO_3$ to have the domain walls oriented parallel to the threefold symmetry axis [13], as preferred. One could expect similar phenomena in $LiOsO_3$. The atom projected PDOS graph [Fig. 2(d)] indicates that the soft mode is associated with all three atoms (Li, Os, and O). The integrated intensities of the imaginary mode are 93%, 4%, and 3% for the Li, Os, and O atoms, respectively. The amplitude of the Os and O atoms and the symmetry consideration give bending of angles and the deviation angle is 178.03°. The deviation angle calculated from the experimental data is about 176.84° as summarized in Table I. Note that the deviation angles for O-Os-O are the same, which is mainly due to off-centering of the Os atom in the [111] pseudocubic direction. One can also see a large displacement value of the Li atoms in this region. However, for the high frequency optical phonon, the contribution of Li is minimal, indicating the weakly bounded state of Li in the crystal lattice. We also have checked the phonon dispersion and atom projected partial PDOS of the optimized $R3c$ phase in Figs. 3(c) and 3(d). Now the phonon dispersion does not show any imaginary frequency, meaning that there is stability of this phase [13,14,30,31]. The contribution from the Li atom appears at around 6 THz, which is the main difference between the two phases. In the highest optical phonon frequency region, again oxygen contribution is dominant. It is important to note that the phonon spectrum of the $R3c$ phase of $LiOsO_3$ is quite similar to that of ferroelectric $LiNbO_3$ [13–18].

We are now in a position to discuss the electronic properties of the two phases. Figures 4(a)–4(c) depict the atom projected DOS of $LiOsO_3$ in two rhombohedral phases near Fermi level. In order to check the DOS, we have done a careful test and our final results for the DOS are given for a dense $20 \times 20 \times 20$ Γ-centered Monkhorst-Pack k-point grid. First of all, the main contribution of the Li atom located in the ~45 eV lower regions from Fermi level and the contribution around Fermi level are 100 times smaller compared to the other two atoms. Note that the scale of Fig. 4(a) is 100 times smaller than that of Figs. 4(b) and 4(c). In other words, oxygen and

TABLE II. Amplimode results of $LiOsO_3$ for the two different phases ($R\bar{3}c$ and $R3c$). The K vector, character, and amplitude of each mode are given. R_{4+} is the octahedral tilting mode responsible for the cubic to $R\bar{3}c$ phase transition and Γ_{2-} (or A_{2u}) is the soft phonon mode associated with the $R\bar{3}c$ to ferroelectric-like $R3c$ phase.

		Reference structure					Displacement	
$LiOsO_3$	Atom	Wyckoff	x	y	z	dx	dy	dz
R_{4+} (from cubic)	Li	6*a*	0.0	0.0	0.25	0.0	0.0	0.0
	Os	6*b*	0.0	0.0	0.0	0.0	0.0	0.0
	O	18*e*	0.1667	0.3333	0.0833	0.0794	0.0	0.0
Γ_{2-} (from $R\bar{3}c$)	Li	6*a*	0.0	0.0	0.25	0.0	0.0	0.0471
	Os	6*a*	0.0	0.0	0.5	0.0	0.0	−0.0088
	O	18*b*	0.3688	0.3688	0.25	0.0027	−0.0027	−0.0128

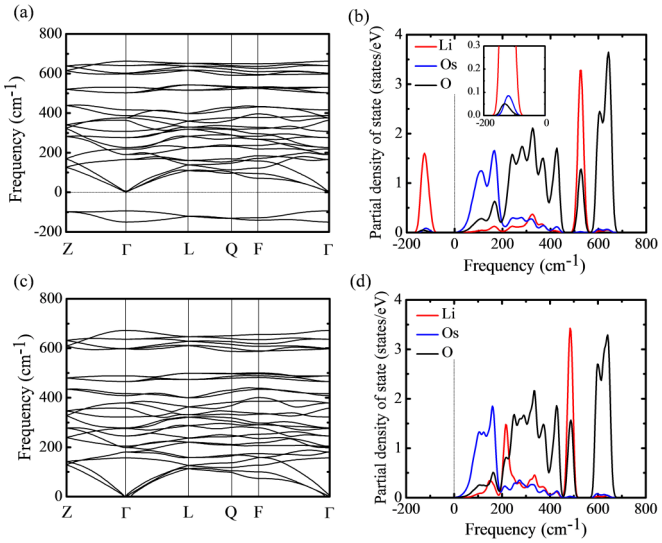

FIG. 3. (Color online) Phonon dispersion curve of $LiOsO_3$ with two different phases along the high symmetry point in the Brillouin zone of the (a) $R\bar{3}c$ room temperature phase and (c) $R3c$ ferroelectric-like phase. Atom projected partial PDOS of the (b) $R\bar{3}c$ room temperature phase and (d) $R3c$ ferroelectric-like phase. The inset of (b) is an enlargement of the imaginary PDOS to show Os and O contributions.

Os hybridization mainly contribute to Fermi level. Secondly, in $LiOsO_3$, the ionic configuration of Os is 5+ and there are three electrons in its d level. The Os partial DOS of $LiOsO_3$ is quite similar to that of $NaOsO_3$ and other osnates [32–35]. Thirdly, at first sight, the atom projected DOS of two phases are nearly identical. However, careful examination

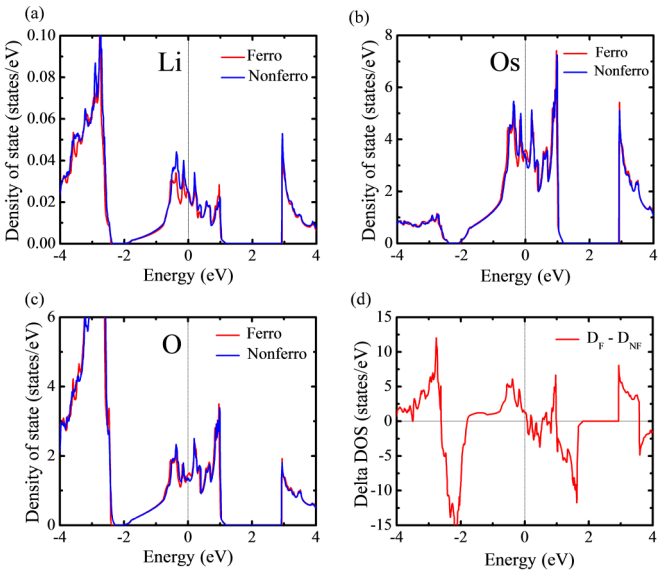

FIG. 4. (Color online) Atom projected electronic DOS of (a) Li, (b) Os, and (c) oxygen atoms. The blue solid line is for the $R\bar{3}c$ room temperature phase and the red solid line is for the $R3c$ ferroelectric-like phase. Note the small y-axis scale of the Li atom. (d) Difference between the total DOS of the $R3c$ ferroelectric-like phase and that of the $R\bar{3}c$ room temperature phase. A plus value means that the total DOS of the $R3c$ ferroelectric-like phase is larger than that of $R\bar{3}c$ at a given energy.

reveals that the DOS at Fermi level for the noncentrosymmetric ferroelectric-like phase is larger. To see this contribution, we have plotted the difference between two total DOS (δ DOS is defined by the DOS for the noncentrosymmetric phase minus the DOS for the centrosymmetric phase) in Fig. 4(d). δ DOS around Femi level is a positive value, which indicates the noncentrosymmetric phase has a larger carrier density around Fermi level. Because the electronic transport of metal is mainly determined by $N(E_f)$ (the number of carriers at Fermi level), the electronic properties have sharp discontinuity at phase transition. From the experimental data of temperature-dependent resistivity, the noncentrosymmetric phase has smaller resistance compared to the centrosymmetric phase. Also one can expect higher susceptibility due to the large number of carriers, and electronic contribution to heat capacity is larger in the noncentrosymmetric phase [8]. We also have checked the band structure and Fermi surface topology (see Supplemental Material Figs. S1 and S2 [29]). The band structures of the two phases are nearly identical with a smaller change near Fermi level, and the Fermi topology [33,35] does not show any drastic change between the two phases. There are, of course, small changes in the symmetry of the hole and electronic Fermi surface and also a smaller change in the cross-sectional area of the Fermi surface, indicating that a de Haas–van Alphen type experiment will show small but clear anomaly across the transition. Also, our electronic structure calculation indicates that the phonon-related transport properties (such as Hall transport, thermal transport, and angle-resolved transport properties) will have significant changes mainly due to two effects: a large change in the phonon structure and a small increase of $N(E_f)$ across the phase transition. Note also that a large thermopower anisotropy has been predicted in a metallic noncentrosymmetric ruthenate oxide system [36].

In conclusion, we have studied the phonon and electronic structure of metallic $LiOsO_3$ based on first-principles density-functional theory. The noncentrosymmetric phase of $LiOsO_3$, $R\bar{3}c$, is closely associated with phonon mode softening and octahedral tilting, which is quite similar to phase transition of ferroelectric $LiNbO_3$-related compounds. A phonon mode of soft phonon (Γ_{2-} or A_{2u}) and octahedral tilting (R_{4+}) is quantitatively analyzed. The soft phonon is the main source of the phase transition from the centrosymmetric to the noncentrosymmetric phase. Due to electron lattice coupling, the density of states near Fermi level increases across this phase transition, which explains the resistivity, heat capacity, and susceptibility changes. For a better understanding of noncentrosymmetric phase transition in this material, soft mode experiments (Raman or neutron scattering) and transport experiments (such as Hall transport, thermal transport, and angle-resolved transport properties) are urgent.

Note added. Recently we noticed that H. J. Xiang computed the local polar distortion and short-range interaction mechanism of $LiNbO_3$ [37]. We also have done a similar calculation, which can be seen in the Supplemental Material [29].

We acknowledge Professor C. Hwang for his help during the calculation. This work was supported by NRF of Korea (Grant No. NRF-2013R1A1A2004496). Computational resources have been provided by KISTI Supercomputing Center (Project No. KSC-2013-C1-029).

[1] M. E. Lines and A. M. Glass, *Principles and Applications of Ferroelectrics and Related Materials* (Oxford University Press, New York, 2001).
[2] E. Bousquet, M. Dawber, M. Stucki, C. Lichtensteiger, P. Hermet, S. Gariglio, J. M. Triscone, and P. Ghosez, Nature (London) **452**, 732 (2008).
[3] J. W. Kim, P. Thompson, S. Brown, P. S. Normile, J. A. Schlueter, A. Shkabko, A. Weidenkaff, and P. J. Ryan, Phys. Rev. Lett. **110**, 027201 (2013).
[4] V. Gopalan and D. B. Litvin, Nat. Mater. **10**, 376 (2013).
[5] M. L. Cohen, Science **261**, 307 (1993).
[6] N. A. Spaldin and W. E. Pickett, J. Solid State Chem. **176**, 615 (2003).
[7] N. A. Benedek and C. J. Fennie, Phys. Rev. Lett. **106**, 107204 (2011).
[8] Y. Shi *et al.*, Nat. Mater. **12**, 1024 (2013).
[9] A. M. Glazer, Acta Crystallogr., Sect. B: Struct. Crystallogr. Cryst. Chem. **28**, 3384 (1972).
[10] P. M. Woodward, Acta Crystallogr., Sect. B: Struct. Sci. **53**, 32 (1997).
[11] P. M. Woodward, Acta Crystallogr., Sect. B: Struct. Sci. **53**, 44 (1997).
[12] C. J. Howard and H. T. Stokes, Acta Crystalloger., Sect. B: Struct. Sci. **54**, 782 (1998).
[13] K. Parinski, Z. Q. Li, and Y. Kawazoe, Phys. Rev. B **61**, 272 (2000).
[14] V. Caciuc, A. V. Postnikov, and G. Borstel, Phys. Rev. B **61**, 8806 (2000).
[15] M. Veithen and Ph. Ghosez, Phys. Rev. B **65**, 214302 (2002).
[16] Y. Okubo Y. Murakami, T. Saito, A. Yokoyama, S. Uehara, and Y. Kawase, Phys. Rev. B **65**, 052107 (2002).
[17] P. Hermet, M. Veithen, and Ph. Ghosez, J. Phys.: Condens. Matter **19**, 456202 (2007).
[18] W. G. Schmidt, M. Albrecht, S. Wippermann, S. Blankenburg, E. Rauls, F. Fuchs, C. Rodl, J. Futhmuller, and A. Hermann, Phys. Rev. B **77**, 035106 (2008).
[19] Q. Peng and R. E. Cohen, Phys. Rev. B **83**, 220103 (2011).
[20] M. C. Rose and R. E. Cohen, Phys. Rev. Lett. **109**, 187604 (2012).
[21] J. P. Perdew, K. Burke, and M. Ernzerhof, Phys. Rev. Lett. **77**, 3865 (1996); **78**, 1396(E) (1997).
[22] G. Kresse and J. Furthmuller, Phys. Rev. B **54**, 11169 (1996).
[23] G. Kresse and D. Joubert, Phys. Rev. B **59**, 1758 (1999).
[24] H. J. Monkhorst and J. D. Pack, Phys. Rev. B **13**, 5188 (1976).
[25] A. Togo, F. Oba, and I. Tanaka, Phys. Rev. B **78**, 134106 (2008).
[26] ISOTROPY, http://stokes.byu.edu/isotropy.html.
[27] D. Orobengoa, C. Capillas, M. I. Aroyo, and J. M. Perez-Mato, J. Appl. Crystallogr. **42**, 820 (2009).
[28] A. A. Mostofi, J. R. Yates, Y. -S. Lee, I. Souza, D. Vanderbilt, and N. Marzari, Comput. Phys. Commun. **178**, 685 (2008); N. Marzari, A. A. Mostofi, J. R. Yates, I. Souza, and D. Vanderbilt, Rev. Mod. Phys. **84**, 1419 (2012).
[29] See Supplemental Material at http://link.aps.org/supplemental/10.1103/PhysRevB.89.201107 for the detailed calculations.
[30] J. M. Rondinelli, and C. J. Fennie, Adv. Mater. **24**, 1961 (2012).
[31] H. Sim, S. W. Cheong, and Bog G. Kim, Phys. Rev. B **88**, 014101 (2013).
[32] Y. Du, X. Wan, L. Sheng, J. Dong, and S. Y. Savrasov, Phys. Rev. B **85**, 174424 (2012).
[33] M. C. Jung, Y. J. Song, K. W. Lee, and W. E. Pickett, Phys. Rev. B **87**, 115119 (2013).
[34] O. N. Meetei, O. Erten, M. Randeria, N. Trivedi, and P. Woodward, Phys. Rev. Lett. **110**, 087203 (2013).
[35] P. W. Silas, P. D. Haynes, and J. R. Yates, Phys. Rev. B **88**, 134103 (2013).
[36] D. Puggioni and J. M. Rondinelli, Nat. Commun. **5**, 3432 (2014).
[37] H. J. Xiang, arXiv:1312.4225.